Automotive Science and Engineering, Vol. 11, No. 3, (2021),3547-3565

Iran University of Science and Technology

Automotive Science and Engineering

Journal Homepage: ase.iust.ac.ir

ISSN: 2717-2023

Numerical investigation of texture density in micro-grooved parallel slider bearing

Amir Hassan Kakaee[1*], Anvar Ahmadkhah[1]

[1] School of Automotive Engineering, Iran University of Science and Technology, Tehran, Iran

ARTICLE INFO

Article history:

Received :

Accepted:

Published:

Keywords:

Friction

Load capacity

Surface textures

Slider bearing

Tribology

A B S T R A C T

Surface texturing modifications improve the tribological performance parameters. In parallel slider bearings with a micro-grooved textured surface, the effects of the Reynolds number and the texture aspect ratio at constant texture density have been studied; however, the texture density variation's effects on the tribological performance have not been investigated yet. The focus of this study is on the texture density variation in micro-grooved parallel slider bearings. The numerical analysis approach was utilized to perform a more in-depth understanding of texture density variation on the two-dimensional pressure distribution, skin friction coefficient, and recirculation zones in micro-grooves and the objective of flow functions such as load-carrying capacity and friction coefficient. In order to validate using the current CFD model for analyzing hydrodynamic bearings, a comparison with the published theoretical paper results was presented. The results were in good agreement with the published theoretical predictions. In a variety of aspect ratios, the texture densities led to an upgrade tribological performance. Results showed remarkable improvements in frictional response with texture density, and an optimal texture density exists. Finally, it was observed that the optimal micro-grooves texture density depends on the texture aspect ratio, while it is independent of the sliding velocity.

[DOI: 10.22068/ase.2021.531]

* Corresponding Author
Kakaee_ah@iust.ac.ir

https://doi.org/10.22068/ase.2021.531

1. Introduction

Using textured surfaces for tribological contact enhancement is not a new concept. For mechanical bearing components, surface texturing has been proven as a means of improving friction and tribological performance both theoretically and experimentally. Meanwhile, surface texturing is applied for the friction coefficient reduction and the wear rate of mating surfaces [1].

Several researchers have employed a variety of numerical models for enhancing tribological performance in terms of load-carrying capacity, friction, and wear [2]. Osborn Reynolds [3] developed the Reynolds equation in 1886 by applying an order-of-magnitude analysis to the Navier-Stokes equations. The method of integrating the Reynolds equation was used for slider bearings with surface discontinuities. In textured sliders, the validity of the Reynolds equation can be decided by the Reynolds number and the texture aspect ratio with equal importance [4]. For a direct wedge bearing, a direct-based model on the conditions of hydrodynamic lubrication was created, and the friction behavior of oil-lubricated, textured steel/sapphire pairs was explained [5]. In [6], using the mathematical model with dimensionless parameters, the relation between textured bearing performance and geometrical/operational parameters was explained.

The theoretical performances of the partially textured bearing were investigated by an adiabatic model [7]. In another research, the tribological influence of texture shape, depth, distance, and diameter behavior of the textured surface in the mixed lubrication regime was studied by an analytical-numerical model [8].

With increasing computational handling power in computer systems, Computational Fluid Dynamic (CFD) is increasingly employed to predict liquid behavior in lubricating situations. Using CFD is valuable since it can give a more common approximation to the Navier-Stokes conditions compared to the Reynolds equation with simple assumptions. The CFD analysis for the tribological properties of Babbitt alloys showed that the main grooves enhance the hydrodynamic effect and the multi-layer surface texture drastically improves the lubricating properties of the Babbitt alloy [9].

In the following, this hydrodynamic effect was solved using the finite element method (FEM), the Stokes equation, and the energy equation in the fluid film for wedge [10]. For plane slider bearings, Rayleigh step bearings, and micro-grooved parallel slider bearings, a finite-element computer program was utilized to solve the Navier-Stokes equations [11]. Using the Finite Cell Method (FCM), the slow computing speed and limited computing scale for multi-scale surface texture hydrodynamic lubrication were resolved [12]. The performance of curved pocket thrust bearings was investigated by implying CFD simulations and conjugate heat transfer at the bearing stator and rotor [13]. Following the previous studies, the tribological performances of the bearing with the compound dimple and simple dimple were studied using a CFD method [14].

For an efficient tribological response function, there are numerous models of deterministic structured textures that permit species to control friction [15]. Meanwhile, the geometrical characteristics and the operating condition affect the performance and wear life of the textured surface of the bearing components [16]. In boundary lubricated textured surfaces, the feed oil capability and wear particles in the interface of a sliding contact are related to the shape, size, and orientation of the texture patterns [17].

Due to their potential in optimizing the frictional behavior, recent studies in tribology continue to improve the microscopic geometry of the textured surfaces. Several studies on surface modifications have exhibited promising outcomes in improving the tribological performance of contacts in hydrodynamic, mixed, and boundary lubrication. In hardened steel, the effect of micro-dimples on the frictional properties was investigated for dimples with different sizes, densities, and geometries [18].

The textured surface application with different shapes at different locations can be a powerful way to improve the performance of bearings [19]. Some researchers have investigated the effects of the geometric features of the pattern on dry sliding friction and on the boundary and/or mixed lubrication [20]. In the powertrain parts, a numerical and experimental study was conducted

[DOI: 10.22068/ase.2021.531]

to explore the capacity of surface structures to diminish grinding between greased-up bearing surfaces[21].

The profitable or badly designed effect of the textured surface is related to the fundamental mechanisms of hydrodynamic pressure generation [22]. Most of the relevant studies have investigated pre-determined shapes and distributions on the textured surface, and no optimum shapes have been obtained. Thus, a deterministic surface micro-texturing is a possibility of altering friction coefficient and wear in the lubrication regime. Therefore, the focus of recent textured surface studies has been on each individual texture shape such that to redesign the textured geometry and density in terms of minimum friction coefficient and maximum bearing load [23]. In order to identify the optimal distribution and parameters of the textures, the influence of textures on tribological characteristics was considered in [24]. Usman and Park worked on the mixed lubrication model to evaluate and optimize the frictional behavior of Piston ring–liner contacts [25]. In the optimization of thrust bearings with commercial software FLUENT, a parametric model of the grooved bottom profile and the GA-SQP hybrid method was used to obtain the optimum profile of the grooved textured bottom [26]. On the bearing, a parametric analysis was conducted to recognize the effect of the main design parameters on the bearing performance [27].

The following conclusions can be made from the previously mentioned works:

(1) The Reynolds equation with its assumptions is weak and not valid for the analysis of fluid flow through hydrodynamic lubrication problems, including those with surface texturing.

(2) The texture profiles, in both indented and anticipated structures, is a significant parameter not only in the bearings but also in surface-textured lubrication.

(3) A wide range of numerical models has been used by many researchers to find optimal texturing parameters for improving the performance of bearings and mating surfaces.

(4) Due to the difficulties of empirical observation of the lubricant behavior in the micrometric dimension range of bearing parameters, using the CFD technique to solve the Navier-Stokes equations seems to be the most appropriate way to account for the optimal distribution and parameters of textures. Accordingly, the numerical investigation of the texture density on micro-grooved parallel slider bearing has not been considered yet. Also, the significance of a 2D numerical study in parallel slider bearing is very important, and the results are not limited to 3D effects. The main explanation for this result is that on this type of bearings, no change occurs in the second texture density in the third coordinate direction, and the 3D flow effects are minimum on the result of numerical simulations.

The main objective of this investigation is to evaluate the mentioned problem and determine the optimal texture density, depending on the texture aspect ratio, to minimize sliding friction coefficient and increase maximum load-carrying capacity.

2. Numerical method

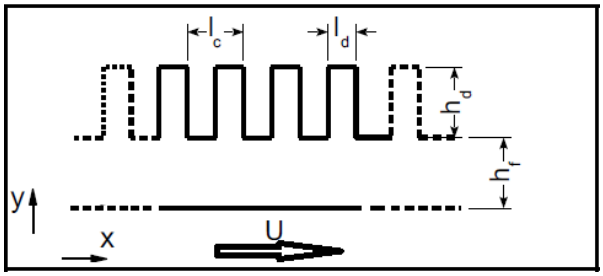

Fig. 1. Geometry for micro-grooved parallel slider bearing

Fig. 1 shows the geometry for the parallel slider bearings with the bearing surface textured with micro-grooves. For textured bearings, an infinite number of grooves were assumed. Due to choosing periodic boundary conditions in isothermal numerical simulation, the cavitation effect was ignored in a symmetrical characteristic of each microgroove unit. Meanwhile, ignoring the cavitation effect made it possible to trait the cause of the cross-film flow parameter variation to the moving wall velocity and geometry.

[DOI: 10.22068/ase.2021.531]

Navier-Stokes equations are solved by making all flow parameter solutions as a function of *x* and *y*. Without thermal interaction, one needs to solve the continuity and momentum equation to acquire velocity and pressure fields. It is assumed that the density is constant, and the viscosity of the fluids does not change with temperature. Then, the equations take the following form:

$$\rho(\nabla.\mathrm{V}) = 0 \qquad (1)$$

$$\rho\frac{\partial V}{\partial t} + \rho(V.\nabla)V = -\nabla P + \mu\nabla^2 V \qquad (2)$$

where ρ is the fluid density, $V = u\,i + v\,j$, μ is the viscosity, and P is the pressure. The flow condition was adjusted by applying different ratios of moving wall speed with respect to texture density. In this equation, $Re = \rho U h_f / \mu$ is in the range of the laminar flow regime.

Table 1 Parameters for surface textured parallel slider bearings.

S	ρ_T	Λ	$U(h_d)$	$Re = \rho U h_f / \mu$
1	0.1	10	Varied	Constant
1	0.3	20	Varied	Constant
1	0.4	30	Varied	Constant
1	0.6	40	Varied	Constant
1	0.7	50	Varied	Constant
1	0.8	60	Varied	Constant
1	0.9	80	Varied	Constant

According to the applied dimensions of surface texturing parameter in parallel slider bearings, the geometrical parameters are set as in Table 1 where $\rho_T = l_d/l_c$ is the texture density, $S = h_d/h_f$ is the groove depth to land film thickness ratio, and $\Lambda = l_d/h_d$ Symbols are the texture aspect ratio [11]. A Familiar FLUENT Multiphysics software was utilized to solve the incompressible Navier-Stokes equations, Eqs. (1) and (2), using the Finite Volume Method (FVM). The least-square cell-based method is used to discretize the governing equations, and the second-order upwind is employed for obtaining flow field velocity [28-30]. For the surface textured parallel slider bearings, periodic boundary conditions are specified for the inlet and exit boundaries. The conditions for the lower surface and the upper surface (bearing) are considered as moving walls for the lower wall and no-slip conditions for the bearing.

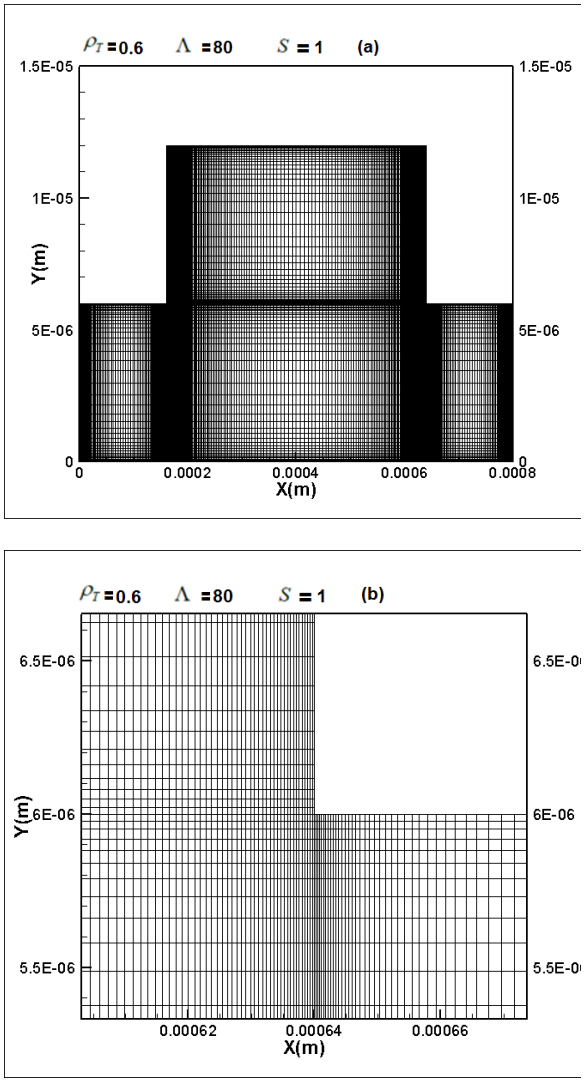

Fig. 2. Mesh of textured slider bearing: (a) entire geometry and (b) around the corner

The constant dynamic viscosity of $\mu = 0.001003\,kg/m.s$ and density $\rho = 998.2\,kg/m^3$ are used in numerical simulations. In Solver parameters, a stationary condition solver is used with the iteration tolerance set to 10^{-5}. Meshes for the textured parallel slider are

[DOI: 10.22068/ase.2021.531]

organized to be clustered around the step corners, as shown in Fig. 2.

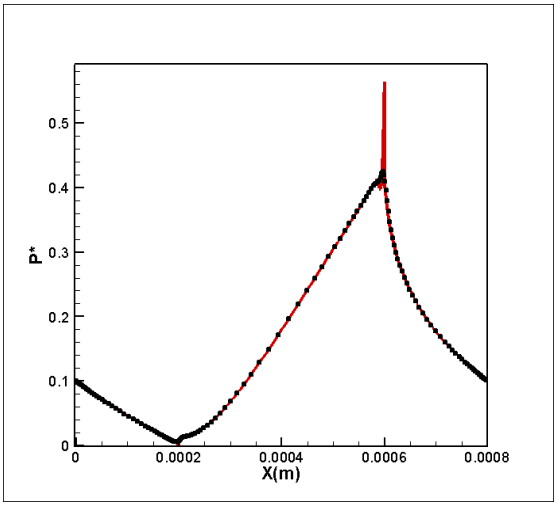

Fig. 3. P^* in the x direction at the moving wall (dotted line) and at $y/h_f = 1$ for a parallel slider bearing with $\Lambda = 40$, $\rho_T = 0.5$, and $s = 1$ for $Re = 1147$

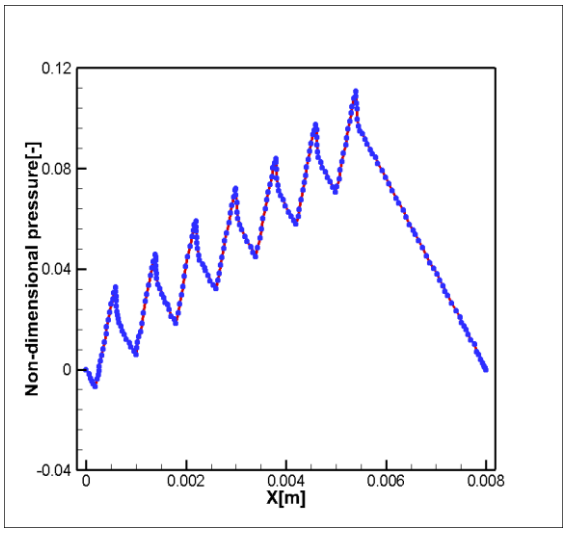

Fig. 4. Pressure distributions along with a somewhat textured parallel slider bearing studied by Dobrica and Fillon [4]; Solid line: the current model; dotted line: Navier-Stokes results from Dobrica and Fillon [4].

The smallest mesh is at the corner, and the sizes of Δx and Δy are 1.38×10^{-3} of l_d and h_d, respectively. Depending on the geometric parameters, the full number of elements is in the range of 120,000 to 360,000 for textured slider bearings. The outcomes are validated by checking the mesh independency. A common measure of quality is based on the equivalent angle skewness, and the mesh quality parameters can also be viewed as graphs. The mesh quality is above 0.145 around the corner. Also, the mean and minimum values for the total domain and mean value are approximately 0.14, 0.009, and 0.156, respectively. A further increase in the number of meshes does not result in distinction in the simulation results. To show the validity of using the current model, we defined the dimensionless pressure P^* as a normalized parameter for micro-grooved parallel slider bearing.

$$P^* = \frac{Ph_f^2}{\mu U l_c} \qquad (3)$$

where P is local pressure, h_f is the land film thickness, μ is viscosity, l_c is texture cell length, and U is the velocity of the moving wall. The validity of using the current FVM model for analyzing hydrodynamic bearings was controlled by simulating a partially textured parallel slider bearing presented in Fig. 3 [11]. Fig. 4 shows the pressure distribution along the moving wall for the current model. As can be seen from Dobrica and Fillon [29], there is an acceptable agreement between the results of the studies.

Figure 5 shows the two-dimensional geometric model of the fluid in the micro-grooved parallel slider bearing with $s = 1$, $\Lambda = 30$, and varied ρ_T. The constant texture cell length and variable textured density parameters of the computational domain used in this study are also shown in Fig. 5. As appeared in Fig. 5, due to the symmetrical characteristic of each microgroove unit, changes within the geometry of the micro-grooves are expanded relative to the middle of the model. In order to facilitate modeling and analysis, the following assumptions are made: 1) The inertia effects are considered; 2) No slip of lubricant is assumed to happen on the boundary, which means the velocity of lubricant close to the friction match surface is identical with that of the

[DOI: 10.22068/ase.2021.531]

friction match surface; 3) Newtonian fluid; 4) Cavitation boundary conditions are not used in this study.

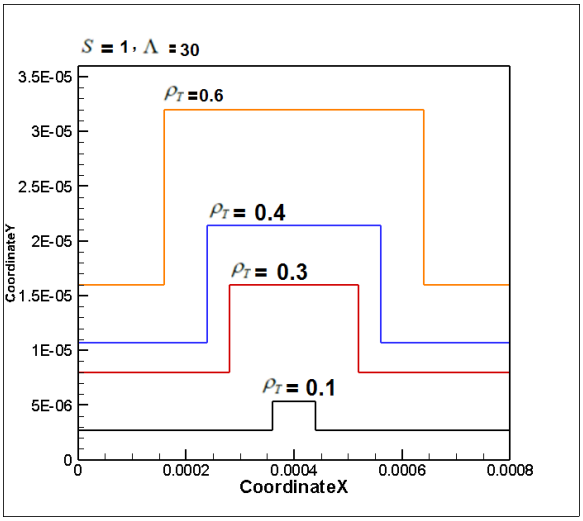

Fig. 5. Geometry for micro-grooved parallel slider bearing with $s = 1$, $\Lambda = 30$, and ρ_T =varied

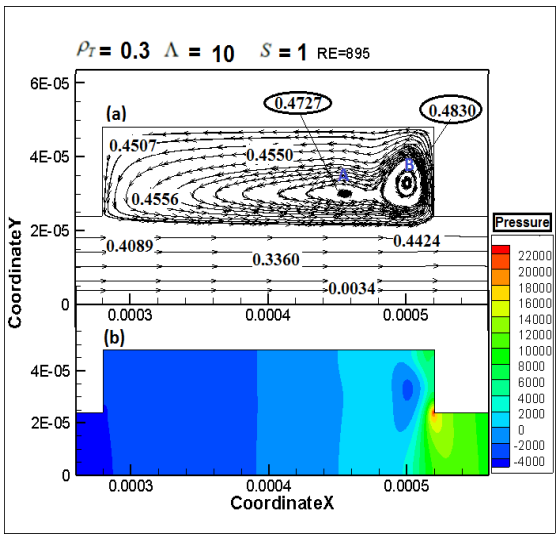

Fig. 6. (a) Streamlines for parallel slider with $s = 1$, $\Lambda = 10$, and $\rho_T = 0.3$ and (b) Pressure distribution of the lubricant

The impact of the micro-groove on the tribological performance of a friction pair under the condition of hydrodynamic lubrication can be characterized by the following tribological parameters: (1); load-carrying capacity force; (2) friction coefficient. The load-carrying capacity force is calculated by integrating the pressure and friction force on the bearing wall over the total calculation domain.

3. Results

3.1 The effect of Reynolds number and texture density on the Two-dimensional pressure distribution and streamline zones circulation

Fig. 6 shows streamlines and pressure distribution of the lubricant in slider bearing. In Fig. 6 (a), there are two recirculation zones (*A* and *B*) similar to another study[11]. Those recirculation zones result from the variety of pressure as appeared from the color maps in Fig. 6 (b). From the illustration, the low pressure in point *A* at x=0.00046, y=0.00003 relative to its encompassing making a centrifugal force field causing the fluid to circle around *A*. Moreover, note that the pressure gradient is very large near the step corner, making an expansive deceleration force for slowing down the local flow; this large pressure gradient also parts the fluid to flow in two opposite *y* directions. Comparing the figures (a) and (b) reveals that the recirculation zones center *B* are nearer to the vertical wall and that the size of the recirculation zone *A* is smaller than the recirculation zone *B*.

[DOI: 10.22068/ase.2021.531]

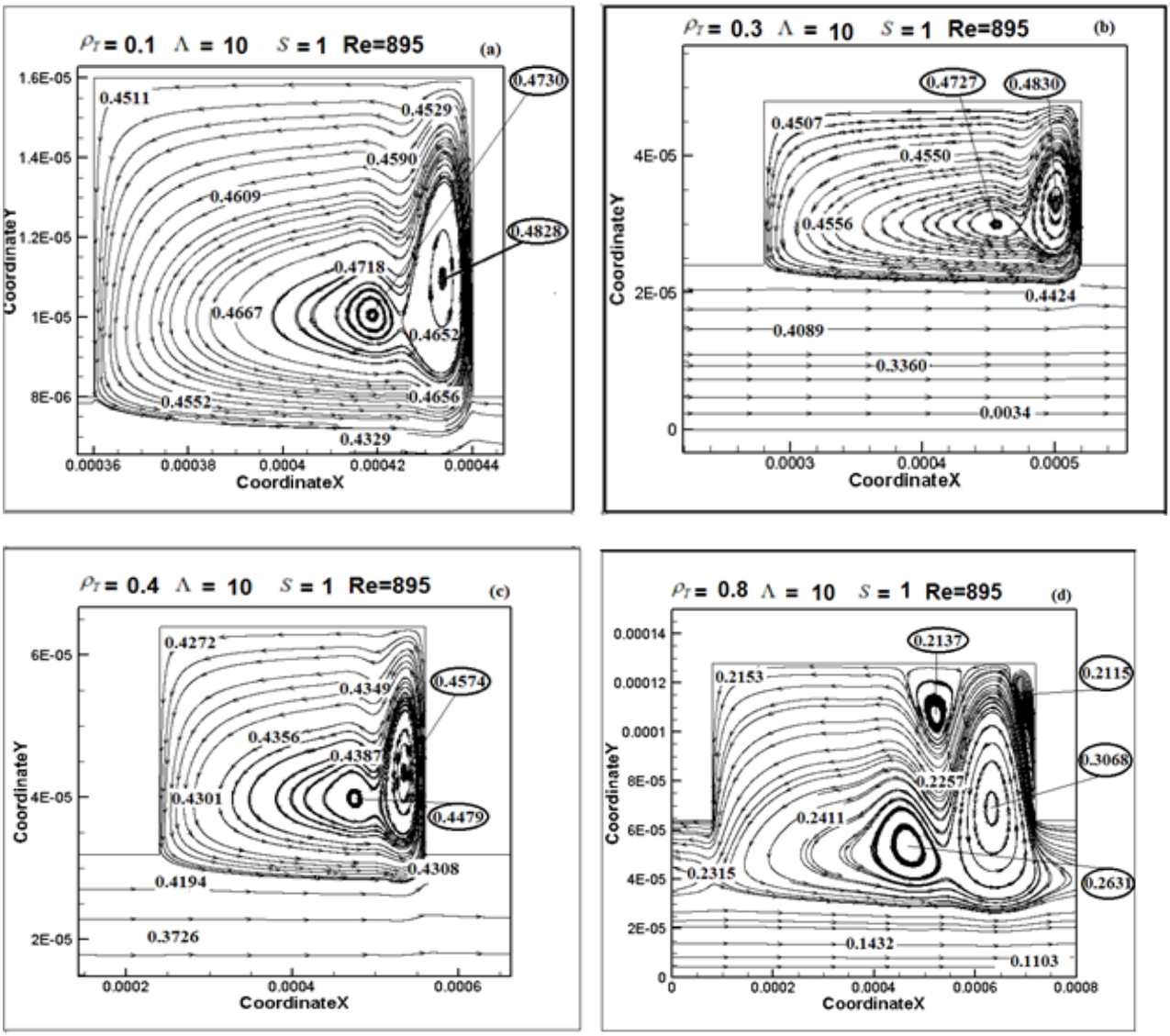

Fig. 7. Streamlines for parallel slider bearings with $s = 1$, $\Lambda = 10$ for (a) $\rho_T = 0.1$, (b) $\rho_T = 0.3$, (c) $\rho_T = 0.4$, (d) $\rho_T = 0.8$.

Fig. 7 shows the streamlines in a groove for $\rho_T = 0.1$, 0.3, 0.4, 0.8 . By comparing the patterns of streamlines, found that the recirculation zones number and center are changed as the ρ_T increases. Meanwhile, the left-most recirculation zone becomes larger and moves to the right with respect to the ρ_T. there is an increasingly longer recirculation zone around the right vertical wall as ρ_T increases. In comparing Fig. 7 (a) and Fig. 7 (d), there are four
recirculation zones for $\rho_T = 0.8$ and two recirculation zones for $\rho_T = 0.1$. The high-pressure gradient near the step corner, creating a large deceleration force for slowing down the local flow; this high-pressure gradient also splits the fluid to flow in four paths in the opposite of *y*-direction. Comparing Figs. 7 (a) and (b), and (c) reveals that recirculation zones are nearer to the moving wall relative to Fig. 7 (d) and that the size of the recirculation is larger than that of the others. Increasing the number of recirculation zones will increase the flow interference, and as a result, the shear force on the bearing wall is increased.

Fig. 8 shows the streamlines in a groove for Re = 895, 1147. Here it is found that the flow gradually becomes complicated as the Reynolds number increases. The right-most recirculation zone

[DOI: 10.22068/ase.2021.531]

becomes larger and moving to the lower wall with respect to *Re*; meanwhile, there is an increasingly larger recirculation zone around the right vertical wall as *Re* increases. In spite of the fact that in larger *Re* number, the shear force on the bearing wall and the flow pressure are increased, but the number of recirculation zones remains constant. As results, within the parameter range of this study, the fluid flow patterns at constant ρ_T are independent of the *Re* number.

Fig. 9 shows the streamlines in a groove for$\Lambda =$ 10, 20, 50 and 60. By comparing the patterns of

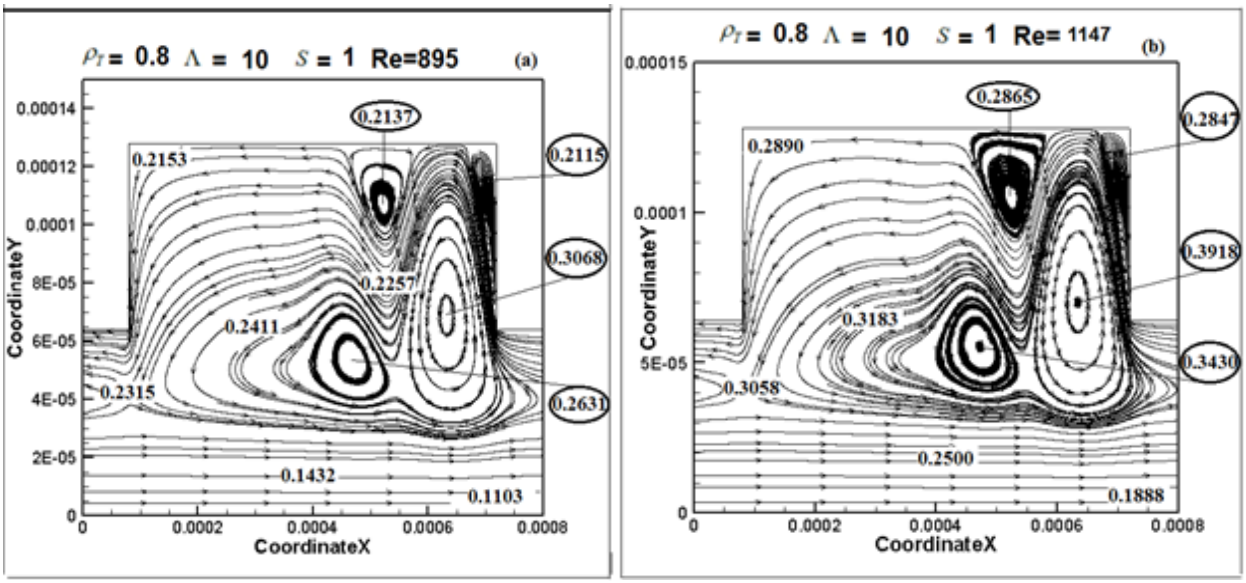

Fig. 8. Streamlines for parallel slider bearings with s=1, Λ=10 and $\rho_T = 0.8$ for (a) Re=895, (b) Re=1147.

streamlines, it is found that the flow becomes less complicated as Λ increased. With increasing Λ, the number of recirculation zone decreases and moving to the left. Meanwhile, in the larger aspect ratio, the size of the recirculation zone around the right vertical wall is increased. Decreasing the number of recirculation zones will decrease the flow interference, and as a result, the shear force on the bearing wall is decreased. In Fig. 9 (a), there are four recirculation zones in $\Lambda = 10$, and In Fig. 9 (b), there are two recirculation zones in $\Lambda = 20$. The size of the recirculation zone near the right wall for $\Lambda = 20$ is much smaller than that for $\Lambda = 10$. From Fig. 9 (c) for $\Lambda = 50$ and Fig. 9 (d) for $\Lambda = 60$, it can be seen that when the texture aspect ratio increased, the left-most recirculation zone becomes larger and moving to the left wall with respect to texture aspect ratio.

3.2 Effect of texture density and aspect ratio on the skin friction coefficient distribution over the moving wall in the groove

One important aim of HD modeling is to precisely predict friction forces. The effects of texture density and aspect ratio on the friction coefficient are shown in Figs. 10-17, respectively. For all cases, these figures show the variation of the skin friction coefficient along the moving wall of the slider bearing.

In these figures, the effects of texture density at constant aspect ratio on the extraction of the least amount of friction force in the one-step of the groove are represented, which are like the outcomes obtained in Refs [31, 32]. The optimum texture density at the constant aspect ratio is determined by integrating the surface area under the skin friction coefficient curves over the

[DOI: 10.22068/ase.2021.531]

moving wall (coordinate X). By comparing the area results, the minimum area value decides the optimal texture density at each aspect ratio. The results of the surface for each aspect ratio are compared, which is similar to the results of the researches represented in Refs [33, 34]. Figs. 10 and 11 show the skin friction coefficient curves relative to the X-axis for different texture densities and $\Lambda = 10\ and\ 20$, respectively.
Comparing the surface areas below the graph for $\rho_T = 0.1$, friction coefficients surface areas increase by 23.23% and 33.33% for $\rho_T = 0.3$ and $\rho_T = 0.4$, respectively. Meanwhile, this increase is more noticeable for $\rho_T = 0.8$, which is equal to 565.65%. The skin friction surface areas for $\Lambda = 10\ and\ 20$ reduce by 1.021% and 30.102% for $\rho_T = 0.4$ and $\rho_T = 0.8$, respectively, which results in a lower friction force for the case $\rho_T = 0.8$ compared to the $\rho_T = 0.1$. Figs. 12 and 13 show the skin friction coefficient curves relative to the x-axis for different texture densities and $\Lambda = 30\ and\ 40$, respectively. As can be seen, skin friction surface areas reduce by 38.846% and 16.153% for $\rho_T = 0.3$ and $\rho_T = 0.6$, respectively, leading to a lower friction force for the case $\rho_T = 0.3$ compared to the $\rho_T = 0.1$.

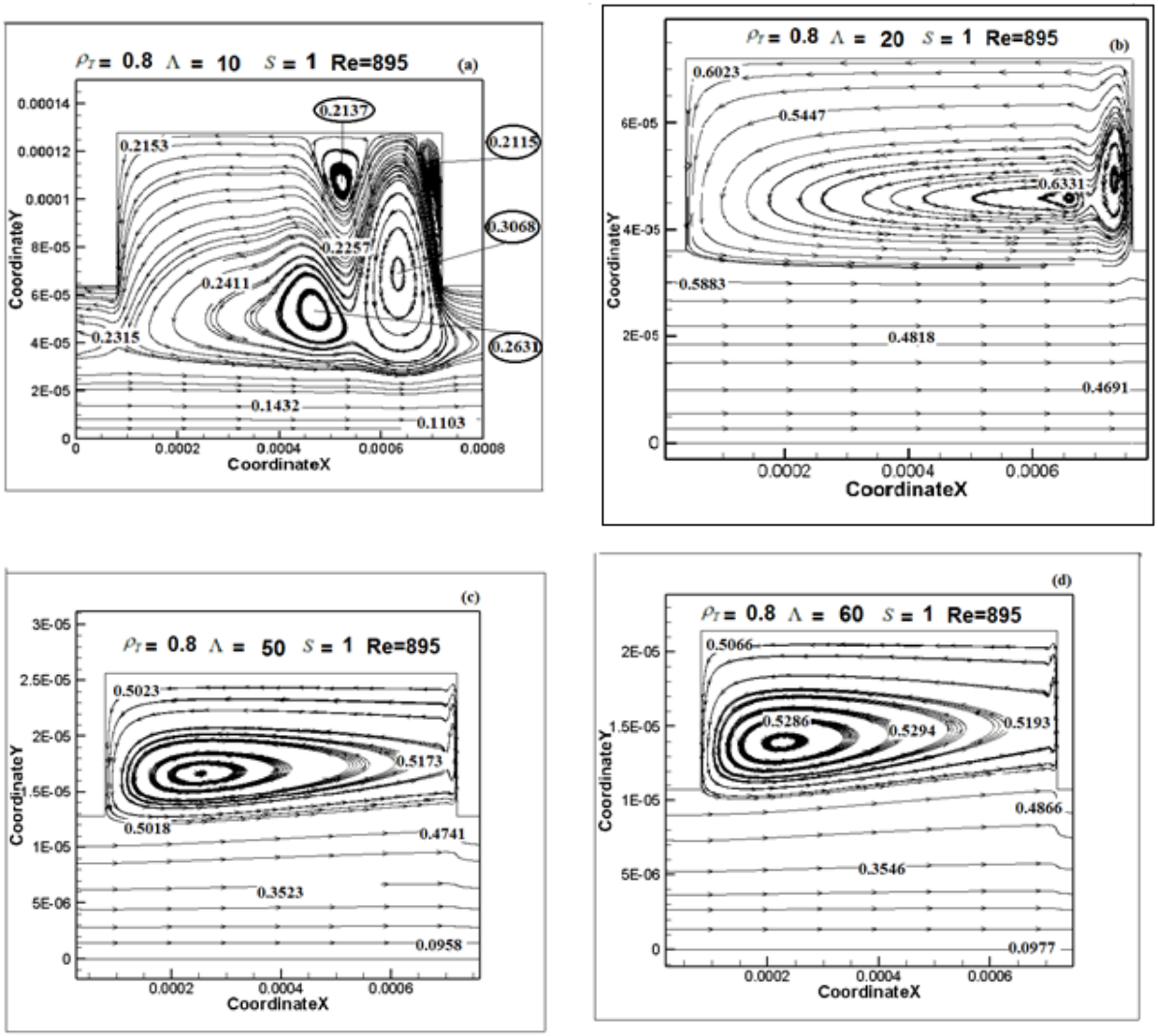

Fig. 9. Streamlines for parallel slider bearings with $s = 1$, $\rho_T = 0.8$ for (a) $\Lambda = 10$, (b), $\Lambda = 20$, (c) , $\Lambda = 50$, (d , $\Lambda = 60$.

[DOI: 10.22068/ase.2021.531]

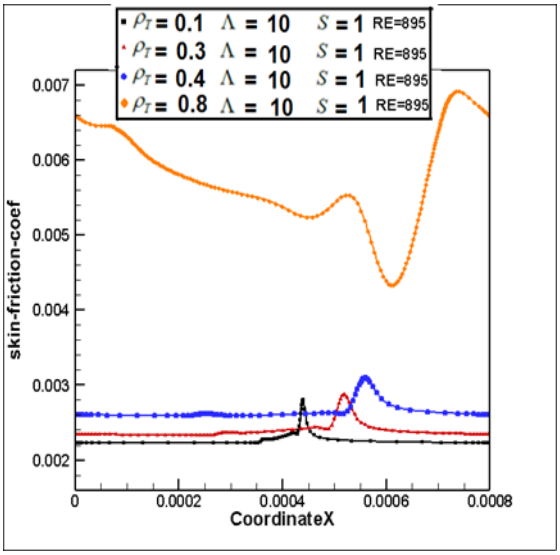

Fig. 10. Skin friction coefficient versus *x* at a moving wall for a parallel slider bearing with $s = 1$, $\Lambda = 10$ and $\rho_T = 0.1, 0.3, 0.4, and\ 0.8$

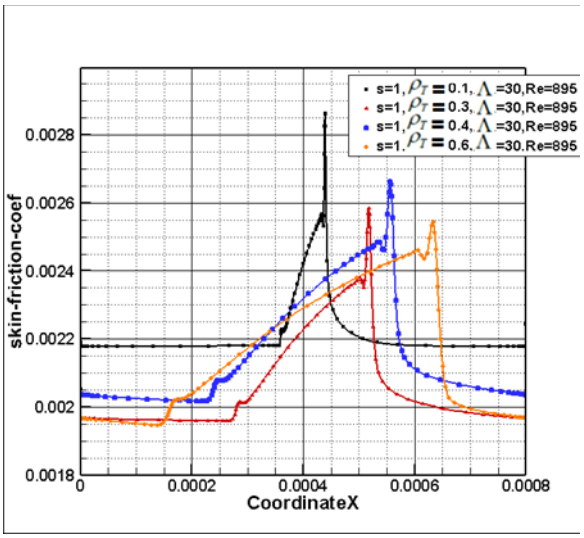

Fig. 12. Skin friction coefficient versus *x* at a moving wall for a parallel slider bearing with $s = 1$, $\Lambda = 30$, and $\rho_T = 0.1, 0.3, 0.4, and\ 0.6$

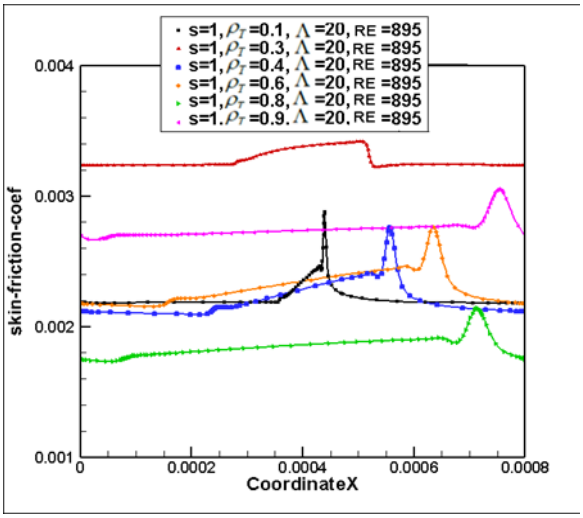

Fig. 11. Skin friction coefficient versus *x* at a moving wall for a parallel slider bearing for $s = 1$, $\Lambda = 20$, and $\rho_T = 0.1, 0.3, 0.4, 0.6, 0.8, and\ 0.9$

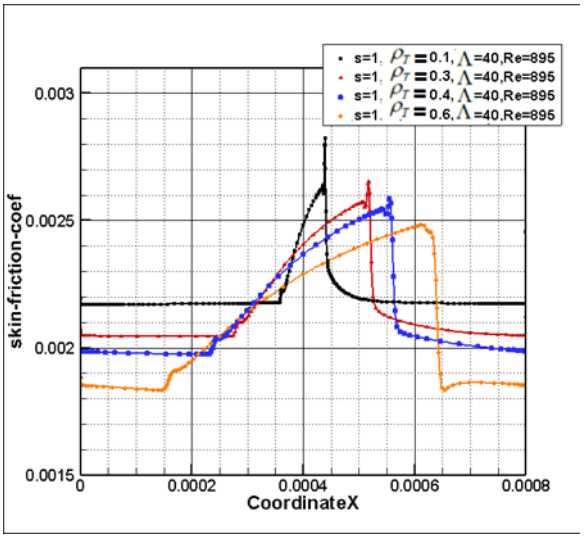

Fig. 13. Skin friction coefficient versus *x* at a moving wall for a parallel slider bearing with $s = 1$, $\Lambda = 40$, and $\rho_T = 0.1, 0.3, 0.4$ and 0.6

The skin friction coefficient surface areas for $\Lambda = 40$ decrease slightly for $\rho_T = 0.3$, $\rho_T = 0.4$, and $\rho_T = 0.6$ compared to the $\rho_T = 0.1$ by 9.012%, 13.344%, and 20.277%, respectively. For $\rho_T = 0.6$, skin friction coefficient surface areas decrease by 20.277%.

Figs. 14 and 15 show the skin friction coefficient curves relative to the x-axis for different texture densities and $\Lambda = 50\ \ and\ 60$, respectively. The skin friction coefficients surface areas decrease for$\rho_T = 0.3, \rho_T = 0.6$, and $\rho_T = 0.8$ compared to the $\rho_T = 0.1$ by 3.937%, 4.461%, and 15.748%, respectively.

[DOI: 10.22068/ase.2021.531]

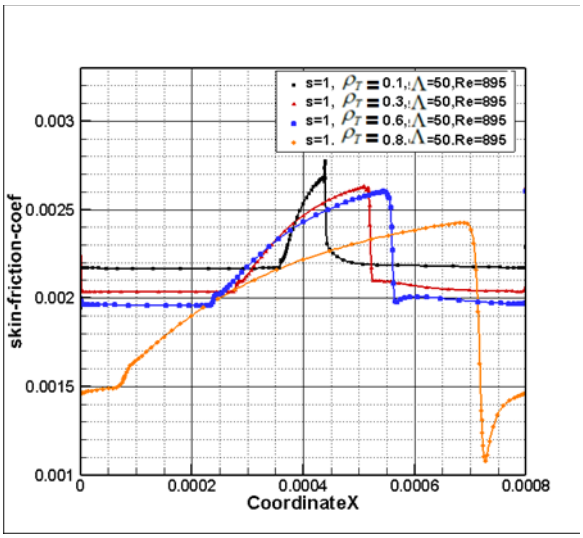

Fig. 14. Skin friction coefficient versus *x* at a moving wall for a parallel slider bearing with $s = 1$, $\Lambda = 50$, and $\rho_T = 0.1, 0.3, 0.6, 0.8, and\ 0.9$

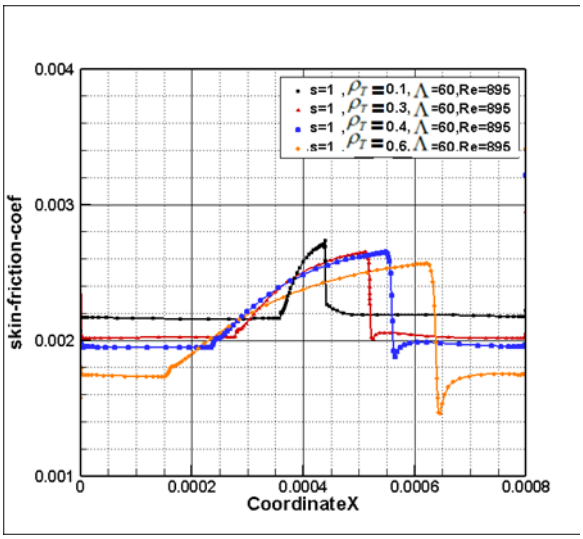

Fig. 15. Skin friction coefficient versus *x* at a moving wall for a parallel slider bearing with $s = 1$, $\Lambda = 60$, and $\rho_T = 0.1, 0.3, 0.4, and\ 0.6$

The skin friction coefficients surface areas for $\Lambda = 60$ decrease for $\rho_T = 0.3, \rho_T = 0.6$, and $\rho_T = 0.8$ compared to the $\rho_T = 0.1$ by 3.703%, 1.058%, and 8.994%, respectively.

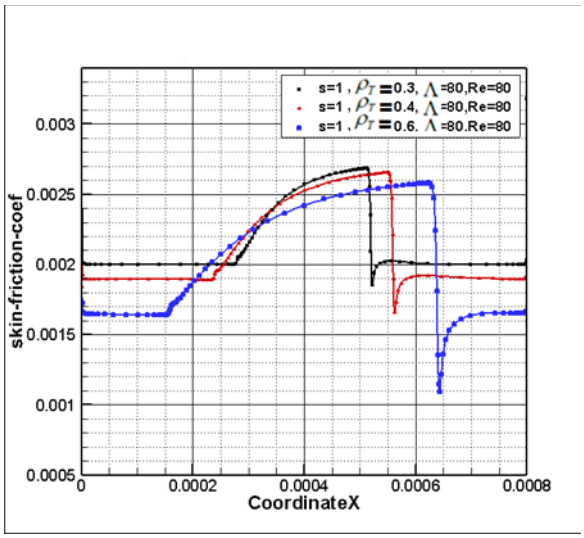

Fig. 16. Skin friction coefficient versus *x* at a moving wall for a parallel slider bearing with $s = 1$, $\Lambda = 80$, and $\rho_T = 0.1, 0.3, 0.4, 0.6, 0.8, and\ 0.9$

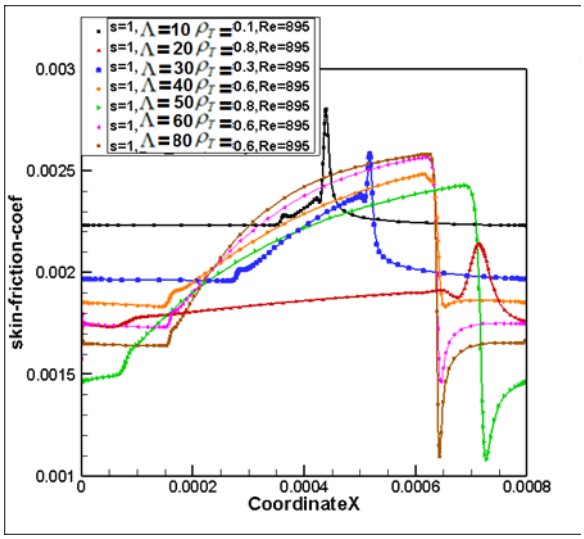

Fig. 17. Minimum skin friction coefficient versus *x* for a parallel slider bearing at different aspect ratios and texture densities

Fig. 16 presents the skin friction coefficient curves relative to the x-axis for different texture densities and $\Lambda = 80$. As can be seen, the skin friction coefficients surface areas decrease for the $\rho_T = 0.4$ and $\rho_T = 0.6$ compared to $\rho_T = 0.3$ by 2.277% and 8.349%, respectively.

[DOI: 10.22068/ase.2021.531]

In Fig. 17, the minimum skin friction coefficient versus *x* is compared for a parallel slider bearing at different aspect ratios and texture densities. Table 2 summarizes the resulting minimum skin friction coefficients surface areas for a parallel slider bearing in different values of Λ and ρ_T. This table presents the results of the lowest value skin friction surface areas. According to the table data, the minimum value of the skin friction surface areas value due to the shear of fluid is for $\Lambda = 20$ and $\rho_T = 0.8$. In addition, as presented in Table 2, this value increases in the skin frictional coefficient surface area, compared with the minimum value as the reference condition ($\Lambda = 20$ and $\rho_T = 0.8$). There is the highest increase in surface areas for texture aspect ratio of 10 and texture density of 0.1 compared to the minimum value by 48.88%.

Table 2. The surface area under the minimum skin friction coefficient curves versus *x* at a moving wall for a parallel slider bearing with micro-grooves with variable texture aspect ratio and texture density

Λ	ρ_T	surface area (minimum)	Percentage of area calculation concerning $\rho_T = 0.8$ and $\Lambda = 20$
10	0.1	997.5e-9	48.88%
20	0.6	670e-9	0
30	0.3	845e-9	26.11%
40	0.6	870e-9	29.85%
50	0.8	780e-9	16.41%
60	0.6	840e-9	25.37%
80	0.6	780e-9	16.41%

3.3. Film pressure distribution of the micro-groove unit

The normal pressure distribution on the lower wall of the lubricant in the micro-groove unit is shown in Fig. 18. As can be noticed, when the lubricant flows into the micro-groove unit from point A to point D, the pressure diminishes steadily and comes to its minimum level at the entry of the micro-groove (point B). At this point, the pressure begins to extend and comes to the greatest at the exit of the micro-groove (point C). From point C to point D, the pressure diminishes to a value at point D, which is identified as point A. Positive hydrodynamic pressure is generated in the merged portion of the groove, while the negative hydrodynamic pressure is produced within the divergent part. With suitable parameters (e.g., texture density and aspect ratio of the micro-groove), the magnitude of the positive pressure is more prominent than that of the negative pressure, which makes the overall integration of the pressure within the micro-groove becomes positive. This phenomenon is the wedging effect of a micro-groove. In this case, the hydrodynamic pressure in the micro-groove unit offers an additional force, leading to an increase in the friction pair's load-carrying capacity.

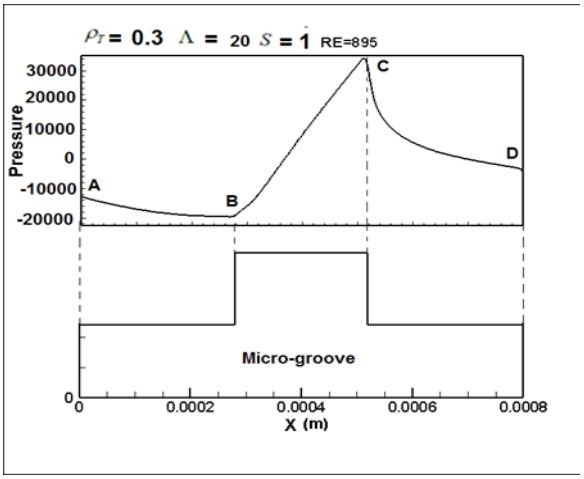

Fig. 18. Pressure distribution versus *x* at moving wall in micro-groove.

3.4. The effect of Reynolds number on the dimensionless pressure distribution P^* at a constant aspect ratio

In this study, the Reynolds number is a function of wall velocity and grooved depth length h_d . Due to the same values of land film thickness and grooved depth length for $= 1$, the calculations are done in constant Reynolds numbers by modifying the velocity of the moving (lower) wall. Fig. 19

[DOI: 10.22068/ase.2021.531]

presents the positive and negative pressure distribution in different values of ρ_T at constant Reynolds number. Based on Figs. 20 (a) and (b), it is seen that the Reynolds number has an insignificant effect on the dimensionless pressure distribution. The magnitudes of the positive and negative dimensionless pressures an increase in the Reynolds number. The increased rate of positive values is higher than that of the negative values. This result indicates that a higher Reynolds number leads to a slight increment in hydrodynamic pressure.

3.5. Effect of texture density and aspect ratio on the load-carrying capacity

Fig. 21 shows the effect of texture density and aspect ratio on the load-carrying capacity (the texture densities of 0.1, 0.3, 0.4, 0.6, and 0.8 are abbreviated as ρ_T=0.1, $\rho_T = 0.3$, $\rho_T = 0.4$, $\rho_T = 0.6$, and $\rho_T = 0.8$, respectively). It is found that for different values of aspect ratio, the load-carrying capacity at $\rho_T = 0.1$ is higher than in other cases. Meanwhile, for a constant texture density, an aspect ratio exists in which the load-carrying capacity force reaches the maximum value. However, the optimum aspect ratio is not constant and changes with the texture density[36-38].

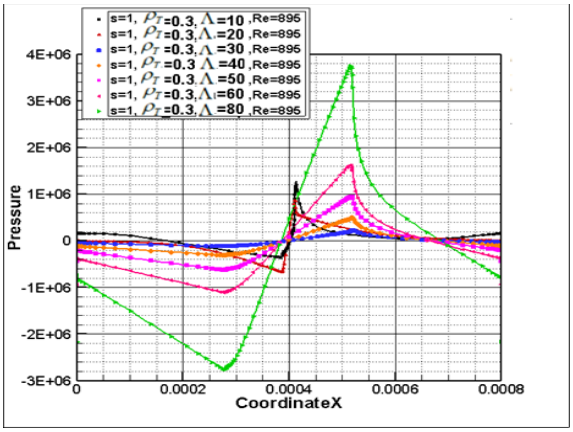

Fig. 19. Effect of aspect ratio on the magnitude of the positive and negative pressure distribution

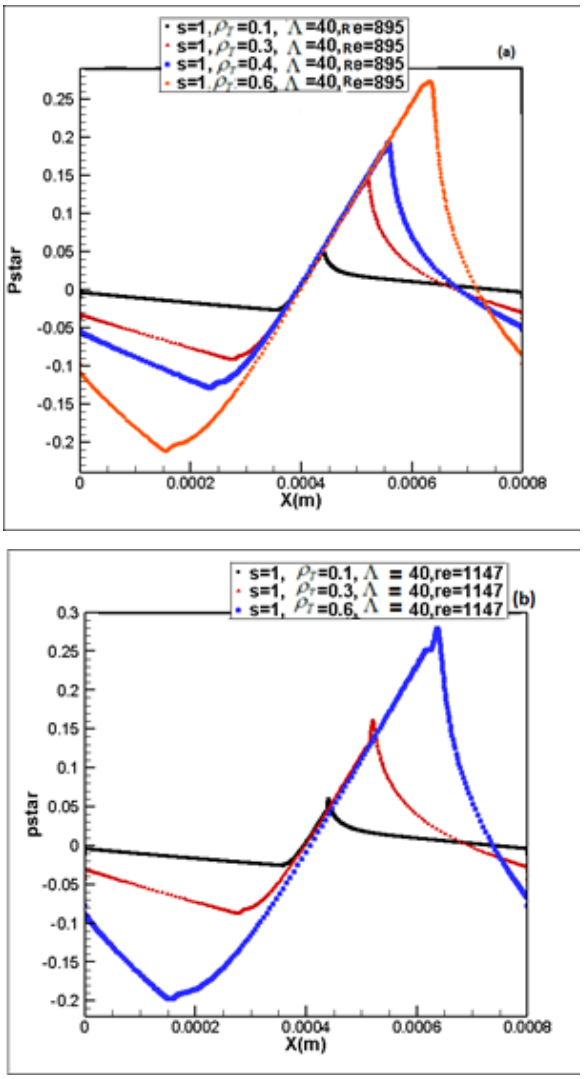

Fig. 20. Effect of Reynolds number on the dimensionless pressure distribution of the micro-groove for (a) *Re*=895 and (b) *Re*=1147

At a constant aspect ratio, an increase in the texture density means that the micro-groove depth increases to a certain value for a constant length of micro-groove. In the previous sections, recirculating flow fields were investigated. Recirculation in microgrooves starts to occur at the top of the micro-groove due to the interaction between the fluid and the micro-groove wall. In terms of energy conversion, a portion of the energy transferred from the moving film lower wall to the fluid is dissipated by being changed over to recirculation's kinetic energy. This phenomenon is called the recirculation effect.

[DOI: 10.22068/ase.2021.531]

With the constant length of the micro-groove, a higher aspect ratio leads to an increase in the load-carrying capacity at a constant texture density. In comparison, in constant aspect ratios, the load-carrying capacity decreases at higher texture density. In numerical simulation and the streamlines in a groove, it is found with an increase in the texture aspect ratio, the number of recirculation zone decreases, and the center of the recirculation zone moves toward the left wall of the micro-groove. This phenomenon increases the high-pressure areas on the groove walls. Consequently, the pressure and viscosity forces increase, which means higher load-carrying capacity. Meanwhile, in a constant aspect ratio, the flow becomes smoothly complicated by increasing the texture density, and the number of recirculation zones in the groove increases with boosts in the flow interaction. This recirculation zone interference reduces the high-pressure area on the walls and decreases the pressure and the viscosity forces.

Fig. 22 shows the effect of texture density and aspect ratio on the load-carrying capacity (the aspect ratios of 10, 20, 30, 40 and 50 are abbreviated as Λ=10, Λ=20, Λ=30, Λ=40, and Λ=50, respectively). It is found that in different texture densities, the load-carrying capacity at Λ=50 is higher than Λ=10, 20, 30, and 40. It is clear that the load-carrying capacity decreases gradually and reaches the minimum value with respect to texture density for a constant aspect ratio. Meanwhile, for a specific aspect ratio increase, both the film pressure force and shear force increase, leading to the maximum load-carrying capacity force. The increased rate in film pressure force is lower compared to that of the film shear force. These conclusions about the load-carrying capacity are consistent with those in another texture-shape study [39].

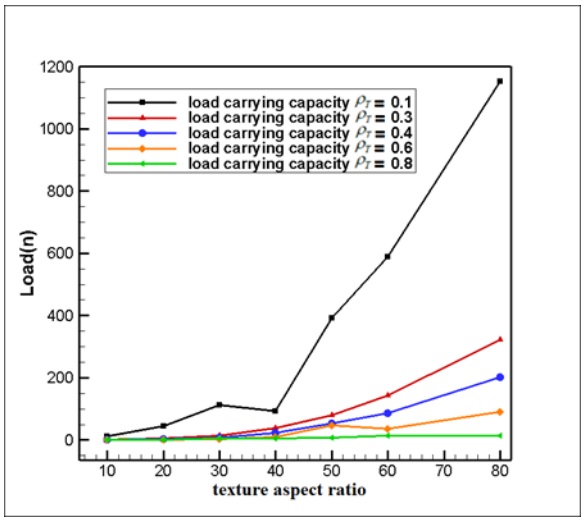

Fig. 21. Effect of texture density and aspect ratio on the load-carrying capacity (with respect to aspect ratio)

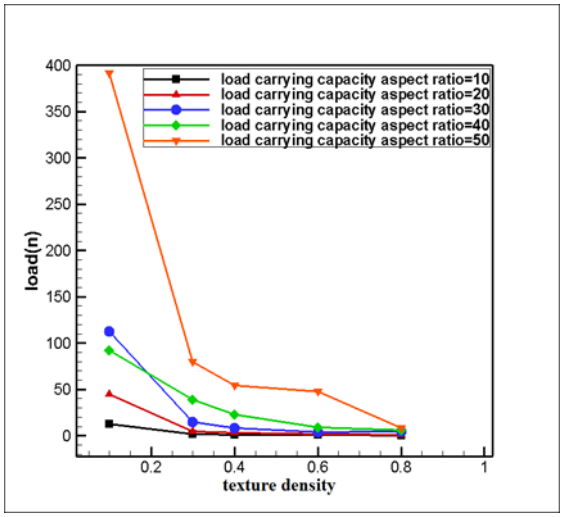

Fig. 22. Effect of texture density and aspect ratio on the load-carrying capacity (with respect to texture density)

3.6. Effect of texture density and aspect ratio on the friction coefficient (respect to aspect ratio and texture density)

Figs. 23-24 show the effect of texture density and aspect ratio on the friction coefficient of the micro-groove bearing. As shown in Fig. 23, there

[DOI: 10.22068/ase.2021.531]

are similar trends for friction coefficient curves for all ranges of aspect ratio. Due to the significant increase in the film shear force at the aspect ratio of 20, the friction coefficient reaches a very high value for all ranges of texture densities [23].

Texture density (Fig. 24) significantly alters the friction coefficient at different aspect ratios. It is found that the minimum friction coefficients decrease by an increase in the values of the aspect ratio. In addition, there are texture density and aspect ratio values that lead to the most appropriate tribological performance for micro-groove bearing. Friction reduction increases by an increase in the aspect ratio, but inside the range of parameters investigated in this study, the values of texture density for the minimum friction coefficient are about 0.4 for the aspect ratio range of 60 to 80.

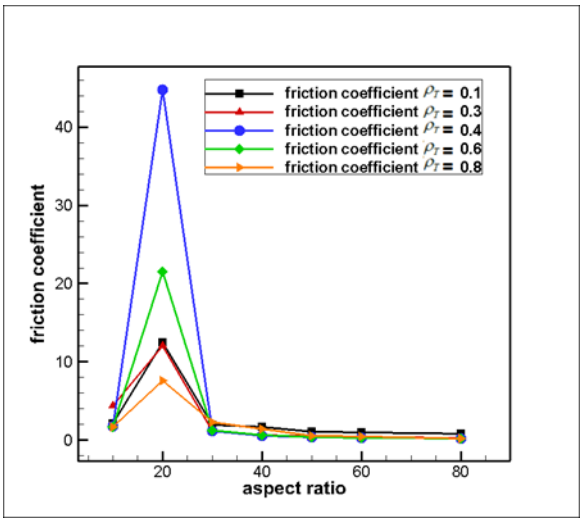

Fig. 23. Effect of texture density and aspect ratio on the friction coefficient (with respect to aspect ratio)

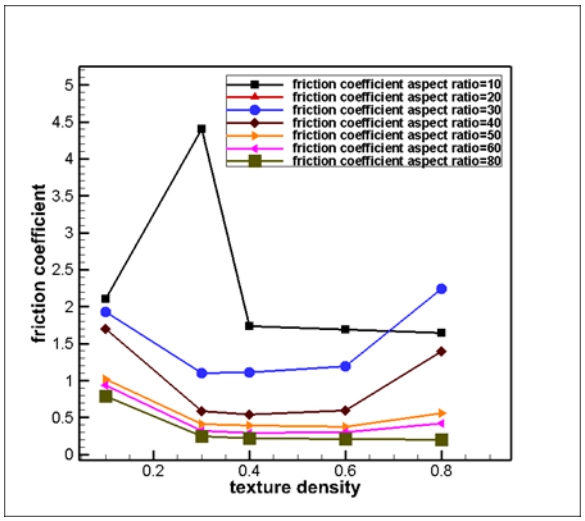

Fig. 24. Effect of texture density and aspect ratio on the friction coefficient (with respect to texture density)

3.7. The combined effect of texture density and aspect ratio on the tribological performance for micro-groove bearing

The combined effect of texture density and aspect ratio on micro-groove bearing's tribological performance is shown in Fig. 25.

In any case of texture density, increasing the micro-groove aspect ratio improves the frictional performance (Fig. 25a). Fig. 26a presents the friction coefficient improvements in the range of texture density numbers between 0.3 and 0.4 for a complete range of aspect ratio. Fig. 25b shows the load-carrying capacity of the micro-groove for tribological performance. As can be noticed, the variation trend of the load-carrying capacity is affected by textured density and aspect ratio. For the bearing's tribological performance, the effects of load-carrying capacity and the friction coefficient must be considered simultaneously. The optimum texture density and the aspect ratio lead to the most good tribological performance for the maximum load-carrying capacity and minimum friction coefficient. Within the range of the parameters investigated in this study, the optimum texture density is found to be 0.1 for an aspect ratio of 80. Increasing the Reynolds number does not show any significant effect on this result.

[DOI: 10.22068/ase.2021.531]

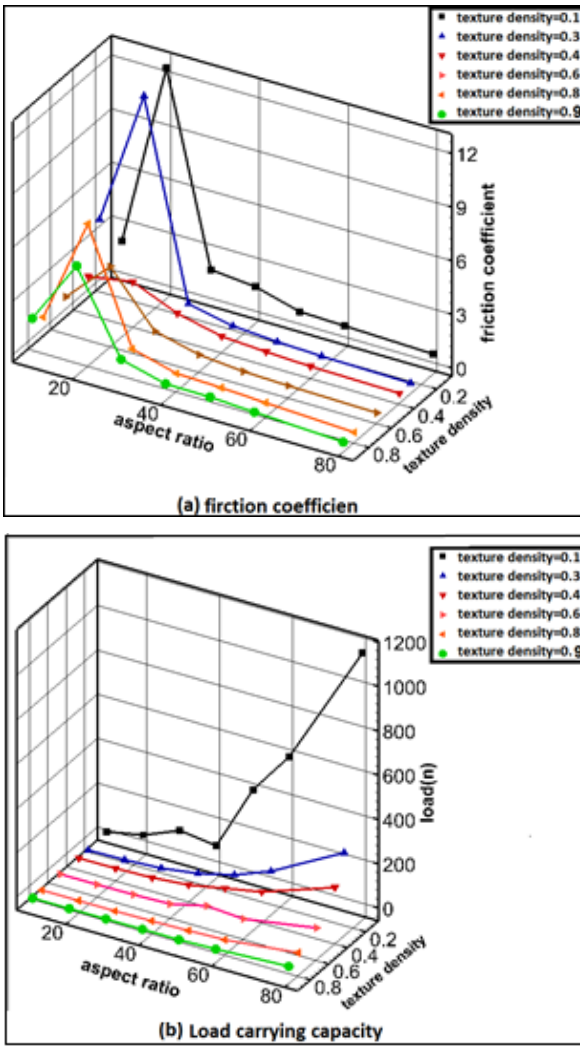

Fig. 25. Tribological characteristics of a micro-groove parallel slider bearing with different geometric parameters of textures density and aspect ratios
Notes: (a) Friction coefficient and (b) Load carrying capacity

4. Conclusions

By utilizing a 2D CFD method, the tribological performance of a micro-groove bearing was examined under hydrodynamic lubrication conditions. The current research focused on the effect of texture density of the micro-groove unit parameters and fluid properties on the tribological characteristics.

Recirculation in microgrooves starts to occur at the top of the micro-groove due to the interaction between the fluid and the micro-groove wall. Meanwhile, the recirculation zone's size around the right vertical wall is increased in the larger aspect ratio. The number of recirculation zone decreases with an increase in the texture aspect ratio. Increasing the number of recirculation zones will increase the flow interference, and as a result, the shear force on the bearing wall is increased.

For the bearing's tribological performance, the effects of load-carrying capacity and the friction coefficient must be considered simultaneously. Texture density significantly alters the friction coefficient, and the minimum friction coefficients decrease by an increase in the aspect ratio values. With the constant length of the micro-groove, a higher aspect ratio leads to an increase in the load-carrying capacity at a constant texture density.

Within the range of the parameters investigated in this study, the optimum texture density for the minimum friction coefficient was found to be 0.4 for the aspect ratio range of 60 to 80. Finally, it was concluded that changes in the Reynolds number within the parameters used in this study do not have a noticeable impact on the optimum texture density and aspect ratio. The conclusions drawn in this work might be promising for further numerical studies in specific applications such as journal bearings with micro-grooves, engine cylinders, and mechanical seals. Our future work will focus on implementing more complex boundary conditions and thermal effects by using the fluid-solid interaction method for the specific application.

List of symbols

h_d	$grooved \quad depth \quad (m)$
h_f	$land\ film \quad thickness \quad (m)$
l_c	$texture \quad cell \quad length \quad (m)$
l_d	$groove \quad length \quad (m)$
L	$length \quad of \quad bearing(m)$
P	$pressure \quad (pa)$
P^*	$non-dimensionalpressure$
RE	$Reynolds \ \ Number$

[DOI: 10.22068/ase.2021.531]

U	$moving\ wall\ \ velocity\ (m/s)$
V	$y-component\ \ velocity\ (m/s)$
x	$the\ slidind\ \ coordinate\ (m)$
y	The cross film coordinate (m)

Greek symbols

Λ	Texture aspect ratio
μ	Viscosity
ρ	Fluid density
τ	Magnitude wall shear
ρ_T	Texture density

References

[1] Marian, V., M. Kilian, and W. Scholz, Theoretical and experimental analysis of a partially textured thrust bearing with square dimples. Proceedings of the Institution of Mechanical Engineers, Part J: Journal of Engineering Tribology, 2007. **221**(7): p. 771-778.

[2] Gropper, D., L. Wang, and T.J. Harvey, Hydrodynamic lubrication of textured surfaces: A review of modeling techniques and key findings. Tribology International, 2016. **94**: p. 509-529.

[3] Reynolds, O., IV. On the theory of lubrication and its application to Mr. Beauchamp tower's experiments, including an experimental determination of the viscosity of olive oil. Philosophical Transactions of the Royal Society of London, 1886. **177**: p. 157-234.

[4] Dobrica, M. and M. Fillon, About the validity of Reynolds equation and inertia effects in textured sliders of infinite width. Proceedings of the Institution of Mechanical Engineers, Part J: Journal of Engineering Tribology, 2009. **223**(1): p. 69-78.

[5] Wahl, R., J. Schneider, and P. Gumbsch, Influence of the real geometry of the protrusions in micro textured surfaces on frictional behaviour. Tribology letters, 2012. **47**(3): p. 447-453.

[6] Rahmani, R., et al., An analytical approach for analysis and optimisation of slider bearings with infinite width parallel textures. Tribology International, 2010. **43**(8): p. 1551-1565.

[7] Marian, V.G., et al., Theoretical and experimental analysis of a laser textured thrust bearing. Tribology letters, 2011. **44**(3): p. 335.

[8] Zhang, H., et al., A mixed lubrication model for studying tribological behaviors of surface texturing. Tribology International, 2016. **93**: p. 583-592.

[9] Zhang, D., et al., Study on tribological properties of multi-layer surface texture on Babbitt alloys surface. Applied Surface Science, 2016. **390**: p. 540-549.

[10] Meng, X. and M. Khonsari, On the effect of viscosity wedge in micro-textured parallel surfaces. Tribology International, 2017. **107**: p. 116-124.

[11] Shyu, S.-H. and W.-C. Hsu, A numerical study on the negligibility of cross-film pressure variation in infinitely wide plane slider bearing, Rayleigh step bearing and micro-grooved parallel slider bearing. International Journal of Mechanical Sciences, 2018. **137**: p. 315-323.

[12] Pei, S., et al., A multi-scale method of modeling surface texture in hydrodynamic regime. Tribology International, 2011. **44**(12): p. 1810-1818.

[13] Fouflias, D.G., et al., Thermohydrodynamic analysis and tribological optimization of a curved pocket thrust bearing. Tribology International, 2017. **110**: p. 291-306.

[14] Meng, F., et al., Effect of compound dimple on tribological performances of journal bearing. Tribology International, 2015. **91**: p. 99-110.

[15] Abdel-Aal, H.A. and M. El Mansori, Tribological analysis of the ventral scale structure in a Python regius in relation to laser textured surfaces. Surface Topography: Metrology and Properties, 2013. **1**(1): p. 015001.

[DOI: 10.22068/ase.2021.531]

[16] Ibatan, T., M. Uddin, and M. Chowdhury, Recent development on surface texturing in enhancing tribological performance of bearing sliders. Surface and Coatings Technology, 2015. **272**: p. 102-120.

[17] Pettersson, U. and S. Jacobson, Friction and wear properties of micro textured DLC coated surfaces in boundary lubricated sliding. Tribology letters, 2004. **17**(3): p. 553-559.

[18] Wakuda, M., et al., Effect of surface texturing on friction reduction between ceramic and steel materials under lubricated sliding contact. Wear, 2003. **254**(3-4): p. 356-363.

[19] Tala-Ighil, N., M. Fillon, and P. Maspeyrot, Effect of textured area on the performances of a hydrodynamic journal bearing. Tribology International, 2011. **44**(3): p. 211-219.

[20] Etsion, I. and G. Halperin, A laser surface textured hydrostatic mechanical seal. Tribology Transactions, 2002. **45**(3): p. 430-434.

[21] Schubert, A., et al., Manufacturing of surface microstructures for improved tribological efficiency of powertrain components and forming tools. CIRP Journal of Manufacturing Science and Technology, 2011. **4**(2): p. 200-207.

[22] Fowell, M., et al., Parametric study of texturing in convergent bearings. Tribology International, 2012. **52**: p. 7-16.

[23] Qiu, M., B.R. Minson, and B. Raeymaekers, The effect of texture shape on the friction coefficient and stiffness of gas-lubricated parallel slider bearings. Tribology International, 2013. **67**: p. 278-288.

[24] Zhang, H., et al., Parametric design of surface textures on journal bearing. Industrial lubrication and Tribology, 2015. **67**(4): p. 359-369.

[25] Usman, A. and C.W. Park, Optimizing the tribological performance of textured piston ring–liner contact for reduced frictional losses in SI engine: warm operating conditions. Tribology International, 2016. **99**: p. 224-236.

[26] Wang, W., et al., Numerical optimization of the groove texture bottom profile for thrust bearings. Tribology International, 2017. **109**: p. 69-77.

[27] Zouzoulas, V. and C.I. Papadopoulos, 3-D thermohydrodynamic analysis of textured, grooved, pocketed and hydrophobic pivoted-pad thrust bearings. Tribology International, 2017. **110**: p. 426-440.

[28] Qin, K., et al., A fluid-structure-thermal model for bump-type foil thrust bearings. Tribology International, 2018. **121**: p. 481-491.

[29] Leonard, B. and S. Mokhtari, ULTRA-SHARP nonoscillatory convection schemes for high-speed steady multidimensional flow. 1990.

[30] Leonard, B., The ULTIMATE conservative difference scheme applied to unsteady one-dimensional advection. Computer methods in applied mechanics and engineering, 1991. **88**(1): p. 17-74.

[31] Tang, Z., X. Liu, and K. Liu, Effect of surface texture on the frictional properties of grease lubricated spherical plain bearings under reciprocating swing conditions. Proceedings of the Institution of Mechanical Engineers, Part J: Journal of Engineering Tribology, 2017. **231**(1): p. 125-135.

[32] Sahlin, F., et al., Two-dimensional CFD-analysis of micro-patterned surfaces in hydrodynamic lubrication. Journal of tribology, 2005. **127**(1): p. 96-102.

[33] Wu, Z., et al., Effect of surface texturing on friction properties of WC/Co cemented carbide. Materials & Design, 2012. **41**: p. 142-149.

[34] Caramia, G., G. Carbone, and P. De Palma, Hydrodynamic lubrication of micro-textured surfaces: Two dimensional CFD-analysis. Tribology International, 2015. **88**: p. 162-169.

[DOI: 10.22068/ase.2021.531]

[35] Li, K., et al., Numerical investigation of the tribological performance of micro-dimple textured surfaces under hydrodynamic lubrication. Beilstein journal of nanotechnology, 2017. **8**: p. 2324.

[36] Uddin, M., T. Ibatan, and S. Shankar, Influence of surface texture shape, geometry and orientation on hydrodynamic lubrication performance of plane-to-plane slider surfaces. Lubrication Science, 2017. **29**(3): p. 153-181.

[37] Yu, H., X. Wang, and F. Zhou, Geometric shape effects of surface texture on the generation of hydrodynamic pressure between conformal contacting surfaces. Tribology Letters, 2010. **37**(2): p. 123-130.

[38] Tang, W., et al., The effect of surface texturing on reducing the friction and wear of steel under lubricated sliding contact. Applied surface science, 2013. **273**: p. 199-204.

[39] Han, J., et al., Hydrodynamic lubrication of microdimple textured surface using three-dimensional CFD. Tribology transactions, 2010. **53**(6): p. 860-870.

[DOI: 10.22068/ase.2021.531]